

Graphical Abstract

Prediction and identification of point defect fingerprints in X-ray photoelectron spectra of TiN_x with $1.18 \leq x \leq 1.37$

Pavel Ondračka, Pauline Kümmerl, Marcus Hans, Stanislav Mráz, Daniel Primetzhofer, David Holec, Petr Vašina, Jochen M. Schneider

Can point defects in TiN be characterized by X-ray photoelectron spectroscopy?

Ab initio calculations predict significant core electron binding energy (BE) shifts for:

- Ti interstitials**
- N tetrahedral interstitial**
- Ti vacancy**

Experimental validation
BE shifts observed as predicted in Ti-deficient TiN_x thin films

Ti vacancy concentration quantified

Prediction and identification of point defect fingerprints in X-ray photoelectron spectra of TiN_x with $1.18 \leq x \leq 1.37$

Pavel Ondračka^a, Pauline Kümmerl^b, Marcus Hans^b, Stanislav Mráz^b, Daniel Primetzhofer^c, David Holec^d, Petr Vašina^a, Jochen M. Schneider^b

^a*Department of Plasma Physics and Technology, Faculty of Science, Masaryk University, Kotlářská 2, CZ-61137 Brno, Czech Republic*

^b*Materials Chemistry, RWTH Aachen University, Kopernikusstr. 10, D-52074 Aachen, Germany*

^c*Department of Physics and Astronomy, Uppsala University, Lägerhyddsvägen 1, S-75120 Uppsala, Sweden*

^d*Department of Materials Science, Montanuniversität Leoben, Franz-Josef-Strasse 18, A-8700 Leoben, Austria*

Abstract

We investigate the effect of selected N and Ti point defects in *B1* TiN on N 1s and Ti 2p_{3/2} binding energies (BE) by experiments and *ab initio* calculations. X-ray photoelectron spectroscopy (XPS) measurements of TiN_x films with $1.18 \leq x \leq 1.37$ reveal additional N 1s spectral components at lower binding energies. *Ab initio* calculations predict that these components are caused by either Ti vacancies, which induce a N 1s BE shift of -0.54 eV in its first N neighbors, and/or N tetrahedral interstitials, which have their N 1s BE shifted by -1.18 eV and shift the BE of their first N neighbors by -0.53 eV. However, based on *ab initio* data the tetrahedral N interstitial is estimated to be unstable at room temperature. We, therefore, unambiguously attribute the N 1s spectral components at lower BE in Ti-deficient TiN_x thin films to the presence of Ti vacancies. Furthermore, it is demonstrated that the vacancy concentration in Al-capped Ti-deficient TiN_x can be quantified with the here proposed correlative method based on measured and predicted BE data. Our work highlights the potential of *ab initio*-guided XPS measurements for detecting and quantifying point defects in *B1* TiN_x .

Keywords: TiN, point defects, XPS, vacancy quantification, N 1s and Ti 2p binding energies, DFT

1. Introduction

B1 titanium nitride (TiN) is a well known material with applications like orthopedic implants [1], wear protection [2] or decorative coatings [3] due to its excellent properties: high hardness, wear resistance [4] and thermal stability [5]. In recent years, novel electrical applications such as solar cell contacts [6, 7] or electrodes [8] have been explored, since TiN possesses high

electrical conductivity. Furthermore, TiN has also attracted some interest for plasmonics applications [9–11] offering an alternative to traditional metals like gold or silver [12]. Properties of TiN_x are significantly influenced by the stoichiometry which is mainly facilitated by point defects: most notably N vacancies for $x < 1$, and Ti vacancies or N interstitials for $x > 1$ [13–15]. Specifically, the presence of both N and Ti vacancies was shown to reduce elastic modulus [16], N vacancies were also shown to reduce the bulk modulus [17] and increase hardness [18, 19]. Importantly, the TiN_x optical performance can be tuned by a stoichiometry changes through both Ti and N vacancy introduction such that it can exhibit plasmonic properties from near infrared to long-wavelength infrared range [10, 20]. Point defects also play an important role during O incorporation [21], in fact Ti vacancies are created during the early stages of oxidation [22, 23]. Therefore, knowledge of the specific point defect state is crucial in understanding the structure–property relationship in (not only) TiN thin films.

Several methods have been used in the past to characterize point defects in TiN, like electron energy loss spectroscopy [13, 16], Raman spectroscopy [23], positron annihilation spectroscopy [24] or Mössbauer spectroscopy [25]. Reliable quantification of point defects TiN, as well as in other derived cubic nitrides, however, still remains a challenge and novel methods are being developed. It was recently shown for $\text{WN}_{0.5}$ that the N vacancies can be imaged at the atomic scale by HRTEM when the vacancy concentrations is high [26], or a method based on atom probe tomography has been proposed to quantify both metal and nitrogen vacancies in TiAlN nanolamella coatings [27], however this approach and its accuracy has been questioned [28].

Our recent work showed that it is possible to detect and even quantify the concentration of Ti vacancies in $\text{Ti}_{1-\delta}\text{O}_x\text{N}_{1-x}$ thin films using X-ray photoelectron spectroscopy (XPS) [29]. This was enabled by guiding the XPS analysis with *ab initio* calculations that allow to precisely predict core electron binding energies (BE) shifts using the density functional theory together with core-hole approaches [30–32]. Such a combined approach can help to explain spectral features observed experimentally [33] and to obtain important information about the structure of the materials [34]. XPS has already been used to characterize the surfaces [35–38] and oxidation [39, 40] of TiN films, since even short exposure to air leads to the formation of oxide and oxynitride overlayer at the surface [41, 42]. As the inelastic electron mean free path in TiO_2 is just ~ 1.5 nm at 1000 eV [43], the surface oxide makes it difficult to obtain information about the unoxidized TiN coating itself and thus about the point defects in the film. For example, it was previously shown that Ti-

deficient TiN_x is exhibiting some shift of N 1s binding energies to lower values [36, 44], however, the specific explanation, whether this is a feature of the film itself or just an effect of the oxide layer, was never clarified. While the straightforward solution to eliminate or greatly reduce the oxygen exposure altogether is to perform the XPS measurements *in situ* [36, 45], recently, capping approaches were developed to prevent oxidation of the TiN films even when the samples are exposed to atmosphere [46, 47]. It was also shown that when the oxidation is small, angle-resolved XPS can be used to distinguish the signal coming from below the oxidized region [45]. Therefore, it is possible to use XPS to obtain information from the bulk-like region of the TiN thin film.

In this work, we will examine a series of Al-capped Ti-deficient TiN_x thin films with $1.18 \leq x \leq 1.37$ deposited using high-power pulsed magnetron sputtering together with density functional theory (DFT) calculations of N 1s and Ti 2p BE shifts induced by various point defects. We will critically assess whether point defects in TiN_x , specifically Ti and N vacancies and interstitials, can be accurately detected and quantified using the *ab initio*-based XPS correlative method proposed here.

2. Methodology

2.1. Experiment

TiN_x thin films were deposited onto Si (100) substrates at floating potential using reactive high-power pulsed magnetron sputtering (HPPMS) of a 50 mm diameter Ti target (99.99 % purity, EVOCHEM Advanced Materials) with an average power density of 9.4 W/cm^2 , 2.5% duty cycle and $50 \mu\text{s}$ on-time. The depositions were performed in a pure nitrogen atmosphere at a pressure of 1 Pa and a target-to-substrate distance of 10 cm for 2 hours. The thin film composition was controlled by varying the substrate temperature systematically, from $T_{\text{substrate}} = 100$ to 400°C in 100°C increments. The base pressure at deposition temperature was for all depositions less than 3.6×10^{-5} Pa. After growth, the as deposited thin films were cooled to room temperature for two hours, while still under vacuum. Subsequently, and before atmosphere exposure, a thin Al capping layer was deposited for 12 s by direct current magnetron sputtering of a diameter-50 mm Al target at 3.9 W/cm^2 power density in Ar atmosphere at 0.5 Pa. The Al capping layer was deposited at room temperature since a pronounced island growth was observed at elevated temperatures. Sputter cleaning behind a closed shutter for at least 2 minutes was performed for both Ti and Al targets before the TiN and Al depositions, respectively. After capping and venting, the samples were immediately transferred to the KRATOS AXIS SUPRA X-ray photoelectron spectrometer

to limit the surface contamination by atmosphere exposure, keeping the total air exposure time below 10 minutes.

The XPS was equipped with a monochromatic Al K_α source and a hemispherical detector. The spectrometer was calibrated with respect to the BE of Au $4f_{7/5}$ (83.9 eV), Ag $3d_{5/2}$ (368.3 eV), and Cu $2p_{3/2}$ (932.7 eV) signals. During spectra acquisition, the base pressure of the system was $< 5.0 \times 10^{-6}$ Pa. No charging effects were observed during XPS measurements. O 1s, Ti 2p, N 1s, C 1s and Al 2p core-level spectra were collected with a pass energy of 20 eV, a step size of 0.1 eV, and a dwell time of 1000 ms in 3 alternating sweeps. Additional high resolution (20 sweeps, 10 eV pass energy, 1 s dwell time, and 0.04 eV step) and angle-resolved XPS measurements (at 0° , 50° , and 70° , 3 sweeps, 20 eV pass energy, 1 s dwell time and 0.05 eV step) were performed for the N 1s region.

For the structural analysis with X-ray diffraction (XRD), a Bruker AXS D8 Discover General Area Detector Diffraction System (GADDS) was utilized. The Cu K_{α} ($\lambda = 1.5406 \text{ \AA}$) X-ray source was set to 40 kV at a current of 40 mA and the incident angle was fixed at 15° .

Ion beam analysis has been performed at the Tandem Laboratory of Uppsala University [48]. Depth profiles of the elemental composition were obtained by time-of-flight elastic recoil detection analysis (ToF-ERDA) using 36 MeV $^{127}\text{I}^{8+}$ primary ions. The ion beam was directed onto the sample at an angle of 67.5° with respect to the surface normal and time-energy coincidence spectra were obtained at an angle of 45° with respect to the primary beam. The detection system is described in more detail in [49] and a segmented gas detector system was employed [50]. Time-energy coincidence spectra were converted to depth profiles with CONTES [51] and all films exhibited homogeneous depth profiles. Sources of uncertainty for ToF-ERDA are the detection efficiency below unity as well as the specific energy loss of primary ions and recoil species [52]. Minimization of such uncertainties can be realized by combining different methods [53]. Thus, ToF-ERDA was combined with Rutherford backscattering spectrometry (RBS) using a 2 MeV $^4\text{He}^+$ primary beam and backscattered ions were detected at an angle of 170° . SIMNRA [54] was used for RBS data analysis. Based on the combination of both techniques—ToF-ERDA and RBS—the total measurement uncertainty was 2% relative of the deduced values. The samples are referenced by their ToF-ERDA/RBS composition throughout the manuscript (e.g., $\text{TiN}_{1.37}$, $\text{TiN}_{1.18}$).

2.2. *Ab initio* modelling

$2 \times 2 \times 2$ TiN supercells with size of 64 atoms and a single-point defect were used for the calculations. The list of point defects considered here consists of N (V_N) and Ti (V_{Ti}) vacancies, N and Ti tetrahedral (I_N^t and I_{Ti}^t), split $(10\bar{1})$ -aligned ($I_N^{(10\bar{1})}$ and $I_{Ti}^{(10\bar{1})}$) and split (111) -aligned ($I_N^{(111)}$ and $I_{Ti}^{(111)}$) N and Ti interstitials [55] as well as of the most stable N Frenkel pair consisting of the N split $(10\bar{1})$ -aligned interstitial with the two N atoms equally distant from the vacancy site ($FP_N^{(10\bar{1})}$) [56]. Furthermore, $3 \times 3 \times 3$ supercell models with a single defect were prepared for V_N and V_{Ti} in order to estimate the influence of the supercell size. The initial models were fully relaxed with respect to atomic positions and cell size and shape using the Vienna *Ab initio* Simulation Package (VASP) [57, 58] DFT [59, 60] code. Projector augmented wave (PAW) pseudopotentials [61] were used with the plane-wave energy cutoff of 500 eV, k -point grid of $5 \times 5 \times 5$ ($3 \times 3 \times 3$ for the larger supercells), and Gaussian smearing method with broadening of 0.1 eV.

Nudged elastic band method [62] as implemented in VASP was used to estimate the migration barrier between neighboring interstitial sites. The calculations ran with the same parameters as the structural relaxations above. We used 5 intermediate images between fully relaxed N in the tetrahedral position and the (111) -aligned split interstitial employing the $2 \times 2 \times 2$ supercells. The images were allowed to be fully structurally relaxed during the NEB calculation. The energy barrier calculated by the NEB method can be used together with the Arrhenius equation to estimate transition rates between different interstitial states at a finite temperature.

The N 1s and Ti $2p_{3/2}$ BEs were calculated as the energy difference between the final state, where a single electron was removed from the specified atom and core level and placed in the valence band, and the initial ground state. Self-consistent DFT calculations were used for both the ground and the final state. The final state always corresponds to the lowest energy state under the constraint of the specific core electron being removed from the core level and placed into the valence band. As a result, the method is able to predict the main XPS peaks. However, spectral features corresponding to additional energy loss events, e.g., the satellite peaks, are not modeled. We note that while the absolute BEs do not correspond to the absolute experimental values by few eV, the relative BE shifts using the same method for $Ti_{1-\delta}O_xN_{1-x}$ were previously found to be in perfect agreement with the experiment [29]. The BE calculations were carried out for every atom in the supercell, leading to ~ 64 core hole calculations per defect model and used the all-electron full-potential Wien2k code with the linearized augmented plane-wave basis set [63]. Atomic muffin-

Table 1: Normalized film compositions as measured by combination of ToF-ERDA and RBS. Traces of O (less than 0.7 at.% in all samples) and Al from the capping layer (less than 0.2 at.% in all samples) were detected as well.

T_{dep} ($^{\circ}\text{C}$)	Ti (at. %)	N (at. %)	x in TiN_x
100	42.2(12)	57.8(12)	1.37(5)
200	42.5(12)	57.5(12)	1.35(5)
300	44.8(11)	55.2(11)	1.23(5)
400	45.8(11)	54.2(11)	1.18(5)

tin radii were set to 1.79 and 1.25 Bohr radius for Ti and N atoms, respectively. The basis size parameter $R_{\text{mt}} \cdot K_{\text{max}}$ of 7.5 and $4 \times 4 \times 4$ k -point grid should guarantee a convergence of better than 0.05 eV for the calculated BEs (while the convergence of the relative energy shifts should be even better). Perdew–Burke–Ernzerhof (PBE) functional was used for all calculations [64]. For the purpose of visualization and comparison with experimental spectra, the discrete calculated binding energies were broadened by Gaussians with $\sigma = 0.3$ eV and the energies were shifted such that the main N 1s peak corresponding to stoichiometric TiN without defects is at 397.3 eV and main Ti 2p_{3/2} peak at 455.1 eV [35]. All DFT calculations are publicly available under the Creative Commons license in the NOMAD Archive [65, 66].

3. Results and discussion

3.1. Film composition and structure

The chemical compositions of all as deposited TiN_x films was characterized by ion beam analysis and are summarized in Table 1. All measured samples are Ti-deficient with respect to stoichiometric $\text{TiN}_{1.0}$ and Ti content is decreasing with the decreasing deposition temperature. Figure 1 shows XRD patterns of the deposited films. All films show a highly textured cubic TiN phase, however, with the decreasing deposition temperature, the intensity of the diffraction peaks clearly decreases and larger peak broadening is observed, indicating smaller TiN crystallites. Additionally, the peak shifts to smaller 2θ angles at lower deposition temperatures, thus corresponding to a lattice parameter increase for films deposited at lower temperatures. However, due to very significant texturing in the films and small grain sizes, the evaluation of stress-free lattice parameter, e.g., by $\sin^2 \Psi$ method, was not possible.

3.2. Capping layer quality

A crucial prerequisite before attempting to detect and quantify defects via XPS is verifying the effectiveness of the deposited capping layer; otherwise, it is difficult to distinguish between the

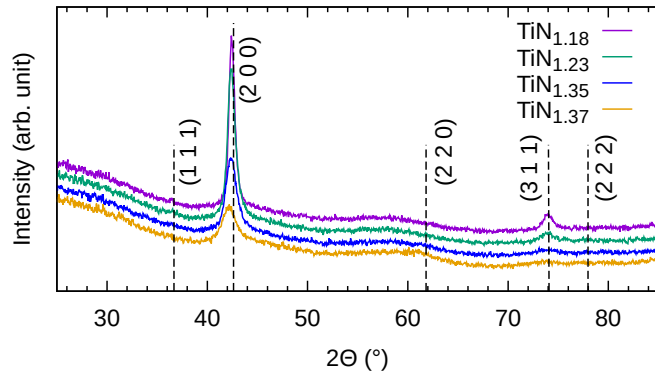


Figure 1: Measured XRD patterns of the TiN_x thin films. The dashed lines show expected diffraction peak positions for stoichiometric cubic TiN (PDF Card No.: 00-038-1420).

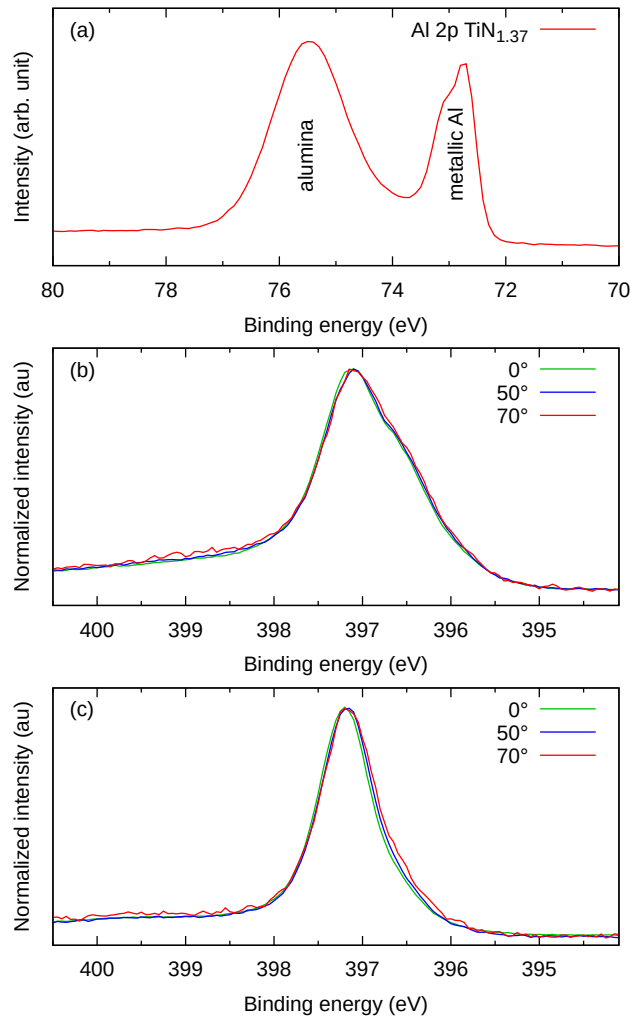


Figure 2: a) Typical Al2p spectrum of the capping layer, similar to what was reported in Ref. [46]. N 1s spectra of b) $\text{TiN}_{1.37}$, c) $\text{TiN}_{1.18}$ at different measurement angles. Measurement angles of 50° and 70° correspond to measurement depths of 64% and 34%, respectively, as compared to measurements at 0° (detector in the direction of the surface normal).

spectral features originating in the surface oxidized layer and in the unoxidized film underneath. An overlayer of TiO_2 and/or TiO_xN_y is formed, when TiN oxidizes. Specifically, the TiO_xN_y surface component was shown to lie ~ 1 eV below the TiN component in the N 1s spectra [42]. Therefore, a two-step workflow was developed to estimate the effectiveness of the Al capping. The first requirement is that the capping layer is thick enough. This was evaluated from the XPS Al 2p spectra, where the contribution from the surface alumina and the remaining metallic Al below can be clearly distinguished. An optimal amount of Al as a compromise between the signal attenuation in the capping and the oxidation protection was determined to be when the alumina and metallic Al peak had approximately the same height, as can be seen in Figure 2 a).

The second important indicator of the Al capping effectiveness is the evolution of the N 1s peak under different XPS measurement angles, shown in Figure 2b) and c) for $\text{TiN}_{1.37}$ and $\text{TiN}_{1.18}$ films, respectively. The differences between the N 1s measurements at different angles are negligible and much smaller than the differences between the different films, which will be discussed later. Since the XPS signals measured at different angles and thus from different depths are virtually identical, we can conclude that the film is homogeneous at the depths probed by XPS and there are no pronounced effects at the capping-TiN interface influencing BEs.

Importantly, if oxidation of the TiN_x film surface would have occurred, it would have resulted in oxygen depth-gradient and, therefore, depth-dependence of the N 1s signal, which is very sensitive to the oxidation [42], should have been identified. As such N 1s signal depth-dependence could clearly not be resolved, it is evident that the Al capping applied here is effectively protecting from oxidation due to atmosphere exposure in the depth range probed by XPS.

In conclusion, the Al capping is effectively protecting all here-reported TiN films from oxidation.

3.3. XPS measurements

XPS measurements of the N 1s spectra of the deposited films are shown in Figure 3a). They exhibit the expected main TiN peak around 397.2 eV as well as weak satellite features at higher BEs [35]. Capped stoichiometric TiN films are expected to only show those two N 1s components [42]. However, with increasing off-stoichiometry, there is a significant shift in the spectral weight from the main TiN-like peak to lower BEs. This is consistent with what was previously reported for Ti vacancies in TiON [29], where this signal originates from N atoms with neighboring Ti vacancies.

Measured Ti 2p XPS spectra are plotted in Figure 3b). The spectra exhibit a structure con-

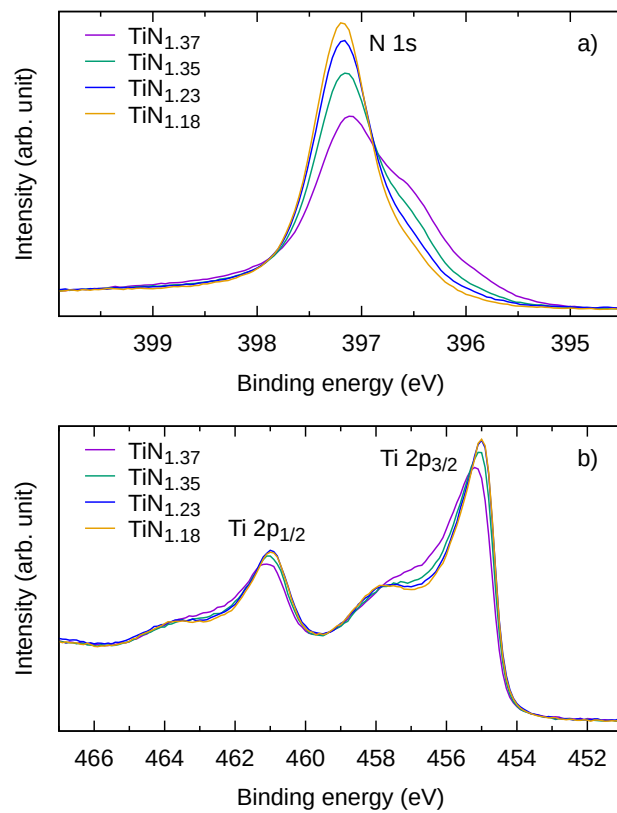


Figure 3: Measured a) N 1s and b) Ti 2p XPS spectra. The curves were scaled to identical peak areas and were aligned by the background to highlight the relative changes.

sisting of four peaks, where the main peaks around 453 eV and 461 eV correspond to the main Ti 2p_{3/2} and Ti 2p_{1/2} peaks of TiN, respectively, and the weaker peaks around 458 and 464 eV are the satellites. No other peaks are observed. Ti 2p BEs exhibit smaller changes with the increasing off-stoichiometry compared to the case of N 1s. There is virtually no difference between the TiN_{1.18} and TiN_{1.23} samples. As the off-stoichiometry is increased, the main peaks shift to slightly higher BEs and there is a small increase in spectra intensity between the main and satellite peaks.

Based on the XRD, ion beam analysis and XPS results as well as previously reported DFT calculations [16, 55, 67], the following, preliminary conclusions about the point defects potentially present in the films can be drawn. There are three possible point defect-based explanations of N excess as measured by the ion beam analysis: Ti vacancies, N interstitials, and N antisites. Ti vacancies have the lowest energy of formation of ~ 3.2 eV [16, 67]. N interstitials have energy of formation of 4.6, 4.8 and 5.46 eV for the split (10 $\bar{1}$)-aligned, split (111)-aligned, and tetrahedral interstitials [55], respectively. The least energetically favorable defect is the N antisite with formation energy of ~ 12.6 eV [16]. Therefore, based on thermodynamic considerations, Ti vacancies are the most probable point defects facilitating the observed off-stoichiometry, due to their low energy of formation. The shift of the XRD peaks to smaller 2Θ angles (indicating increasing lattice parameter) for films deposited at lower temperatures with respect to the films deposited at higher temperatures and also to the powder TiN values, i.e., PDF Card No.: 00-038-1420, may indicate the presence of N interstitials. However, since it was not possible to determine the equilibrium lattice parameter, it is possible that the XRD peak shifts are caused by differences in residual stress states of the films. Therefore, based on the ion beam analysis and XRD data, the presence of N interstitials appear possible but cannot be proven.

In the next step, we critically appraise the above presented hypotheses, i.e., the probable presence of Ti vacancies and/or N interstitials in the as deposited films, based on *ab initio* calculations of the influence of specific point defects on the binding energies of the surrounding atoms.

3.4. *Ab initio* modeling

3.4.1. Core electron binding energies

In the following, we will exclusively discuss the BEs of N 1s and Ti 2p_{3/2} electrons. The point defect visualizations, BE histograms and broadened BEs, as well as the mean BE shifts are summarized in Figure 4 for all the here studied point defects. Only atoms with core electron BE shifts (> 0.15 eV) are marked in the figures. We note that this chosen BE shift limit is to large extend

arbitrary and the experimental resolvability of specific spectral components depends on multiple conditions, most notably the instrumental resolution, temperature, crystalline quality (structure disorder), signal-to-noise ratio and intensity ratios of the components. In the case of the here studied films, the FWHM of the main N 1s spectral component is in the range of 0.65–0.8 eV (as shown in Table 3 which will be discussed in more detail later) for the measurements at 10 eV pass energy. As a very crude estimate, two components could be resolved if their BE difference is at least half of this FWHM value. Therefore, not all of the bellow discussed BE shifts can be resolved by the spectrometer employed in the present work and furthermore, not all the discussed point defects are expected to be present in the here experimentally studied TiN_x with $1.18 \leq x \leq 1.37$. Specifically, presence of Ti interstitials or N vacancies is unlikely, for reasons discussed below. Nevertheless, the following section is an overview of which point defect induced BE shifts are relevant for the experimental analysis of point defects in TiN TiN_x (both $x \geq 1$ and $x \leq 1$) by XPS, assuming in some cases a better instrumentation, e.g., a synchrotron-based XPS.

N vacancy (Figure 4, first row): The second nearest $\text{N}^{2\text{n}}$ neighbors of the vacancy see a slight increase in BEs by around 0.29 eV. This is consistent with previous ELNES calculations, where the influence of N vacancy was also reported to be strongest for the second nearest N neighbors [69]. Other N atoms considered here show BE changes < 0.1 eV and are hence not resolvable with laboratory XPs systems. While the N vacancies introduce a positive shift in BEs of its six first $\text{Ti}^{1\text{n}}$ neighbors, the shift magnitude is only 0.23 eV, and is therefore challenging to be resolved experimentally. The shift of BEs of the second nearest N vacancy N neighbors is larger with almost 0.3 eV. However, the position overlaps with the very broad N 1s satellite peak observed in experiments [35, 42], which is not possible to be modeled by our DFT approach. This complicates fitting and introduces further potential uncertainties.

N tetrahedral interstitial (Figure 4, second row): The interstitial N^{i} atom exhibits a reduced BE of 1.18 eV, while a BE reduction of 0.53 eV was predicted for its first $\text{N}^{1\text{n}}$ neighbors. Both BE shifts of -0.53 eV and -1.18 eV are resolvable by laboratory XPS systems. All other N and Ti atoms are predicted to exhibit unresolvable BE shifts.

N split ($10\bar{1}$)-aligned interstitial (Figure 4, third row): The two split interstitial N atoms show a BE increase of 0.46 eV. The first N^{a} neighbors in the direction of the N_2 bond exhibit a reduced BE by 0.31 eV. The first N^{b} neighbors perpendicular to the N_2 bond see a BE increase of 0.19 eV. The rest of N atoms exhibits a BE shift smaller than 0.1 eV. The two Ti^{a} atoms directly above and

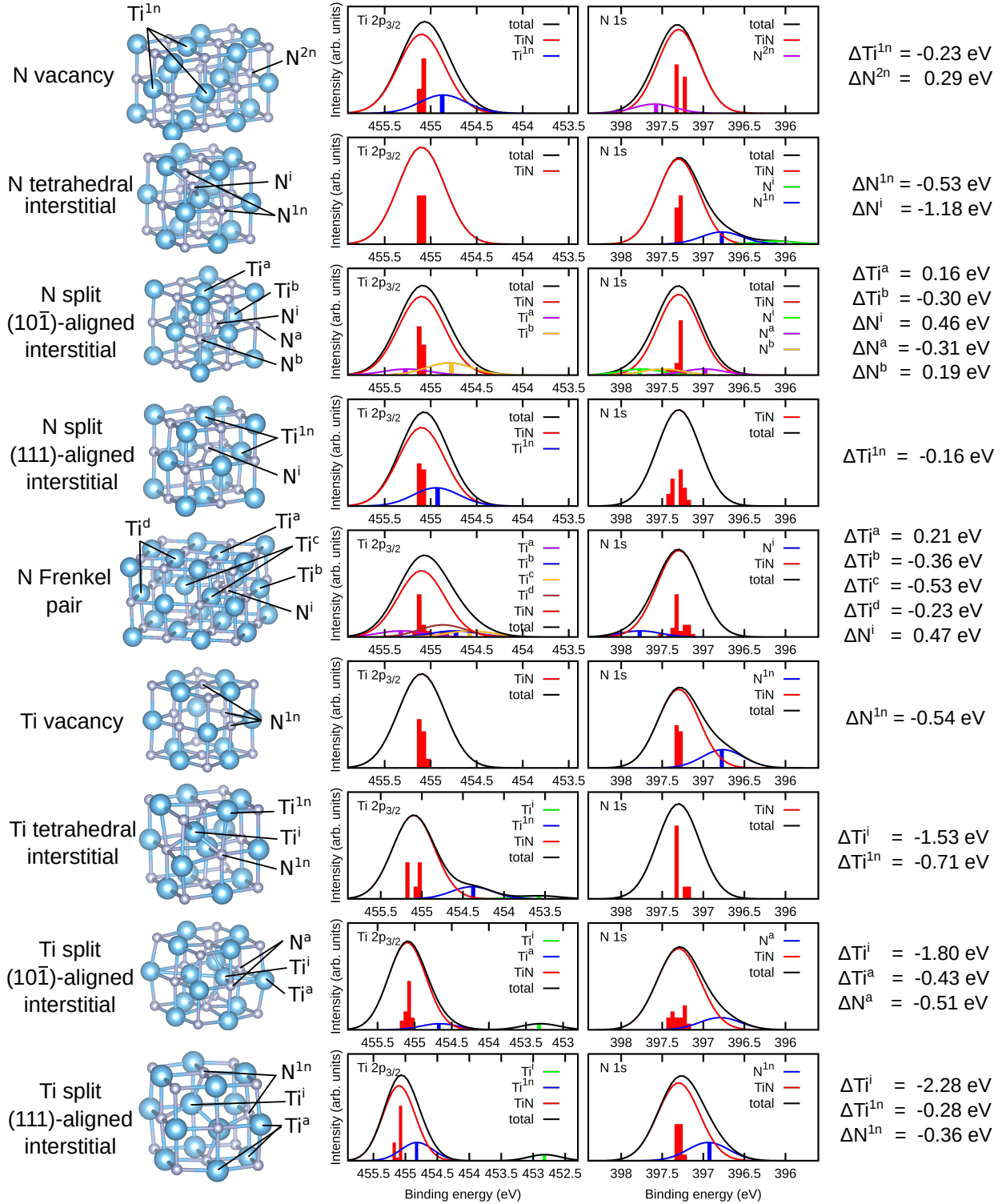


Figure 4: First column: atomic structures (visualized by VESTA [68]) of the here studied defects with marked atoms exhibiting significant BE shifts. Second and third column: histogram and broadened BEs of Ti 2p_{3/2} and N 1s, respectively. Red lines (marked “TiN”) correspond to all remaining atoms in the supercell, which were not specifically highlighted due to having none or negligible BE shifts. Fourth column: Calculated mean BE shifts with respect to the stoichiometric defect-free TiN (the mean energy of the remaining atoms). The nomenclature of labeling sites is explained in the corresponding parts of the text.

below the N_2 bond exhibit increase of BE by 0.16 eV, while the remaining four first Ti^b neighbors see decrease of BE by 0.3 eV. The BE shift of the interstitial N atom of 0.46 eV is resolvable by laboratory XPS, however, the signal is weak as it originates only from two atoms per defect. Potential characterization would be further complicated by an overlap with the satellite peak, which is also situated at higher BE and, therefore, this type of interstitial could be difficult to be unambiguously resolved by fitting extra spectral components.

N split (111)-aligned interstitial (Figure 4, fourth row): There is no N atom with a BE shift ≥ 0.15 eV and the shift of the Ti first neighbors is only -0.16 eV. Therefore, this type of N interstitial is expected to only lead to small peak broadening and, thus, is deemed to be undetectable by XPS.

N Frenkel pair (Figure 4, fifth row): The calculated Frankel pair defect consists of the N split ($10\bar{1}$)-aligned interstitial and a close N vacancy in the direction perpendicular to the N–N bond. The calculated BE shifts are very close to what would be expected from just adding together the effects of the before-calculated N vacancy and N split ($10\bar{1}$)-aligned interstitial. The two interstitial atoms N^i have their N 1s BE increased by 0.47 eV (as compared to 0.46 eV for the separate interstitial). The first Ti^a and Ti^b neighbors of the interstitial exhibit Ti shifts of 0.21 eV and -0.36 eV, respectively, which is similar to the influence of the interstitial alone. A similar effect is seen for the first Ti^d neighbors of the vacancy, where a BE decrease of 0.23 eV is predicted (identical to the effect of the vacancy alone). Two Ti^c atoms, which are both first neighbors of the vacancy and interstitial, exhibit a BE shift of -0.53 eV. In this case, the shift is the exact sum of the effects calculated for N vacancy -0.23 eV and N interstitial -0.3 eV.

Ti vacancy (Figure 4, sixth row): N^{1n} atoms directly next to the Ti vacancy have reduced BEs by 0.54 eV with respect to the rest of the N atoms and the signal is strong as a single vacancy influences 6 N atoms. This interpretation is consistent with the previously published predictions for TiON [29], where it was additionally published that the BE shift is approximately additive with respect to the number of vacancies and that the effect can be used for Ti vacancy quantification using the XPS. The BEs shifts of the Ti atoms ≤ 0.1 , eV, are unresolvable by laboratory XPS.

Ti tetrahedral interstitial (Figure 4, seventh row): This Ti interstitial induces unresolvable changes in the N 1s BEs of the surrounding N atoms. However, the interstitial Ti^i atom itself exhibits BE reduction by 1.53 eV and its first 4 Ti^{1n} neighbors see a BE reduction of 0.71 eV.

Ti split ($10\bar{1}$)-aligned interstitial (Figure 4 eighth row): The only significantly influenced N atoms are the nearest N^a neighbors in the (100) plane, while no other calculated N 1s binding

energies stand out. The general distribution of the remaining BEs from N atoms is quite broad. This is expected as Ti introduces a much larger overall displacements than the smaller N interstitials. The two Ti^i interstitial atoms show a decrease of binding energy by 1.80 eV, Ti^a atoms in the direction of the Ti–Ti interstitial pair bond have BEs reduced by 0.43 eV, and the rest of Ti atoms is unaffected.

Ti interstitial 111 (Figure 4, ninth row): The first 6 N^{1n} neighbors of the Ti interstitial pair have their BEs reduced by 0.36 eV. Other N atoms see no significant change. Two Ti^i interstitial atoms exhibit a BE decrease of 2.28 eV and the Ti^{1n} first neighbors exhibit a BE decrease of 0.28 eV.

Importantly, the predictions highlight that all Ti interstitials exhibit a distinct signal in the Ti 2p spectra. Although the presence of Ti interstitials is quite unlikely due to having very high formation energy of more than 11 eV [67], so N vacancies are more likely in the case of Ti-rich stoichiometry, there are no other overlapping signals at lower BEs with respect to the Ti 2p TiN signal. Therefore, even very small Ti interstitial concentrations should be detectable by laboratory XPS.

In general, the fitting of Ti 2p peak is challenging due to the overlap between the $\text{Ti } 2p_{1/2}$ and $\text{Ti } 2p_{3/2}$ peaks and the presence of satellite peaks which are much more pronounced than in the N 1s signal. The choice of background fitting function and also the choice of a proper asymmetric line shapes is crucial [42]. Based on the discussion above, it is expected that only the Ti interstitials are readily identifiable from the Ti 2p spectra.

Regarding the analysis of the N 1s spectra, we predict a possibility of detecting point defects, which induce a significant negative BE shift of the N 1s atoms, such as Ti vacancies or N tetrahedral interstitials as there is no overlapping peak at lower BEs (assuming the film can be protected from oxidation [42]). Nevertheless, it seems difficult to distinguish Ti vacancies and N tetrahedral interstitials from the XPS spectra. Selected Ti interstitials also induce negative BE shifts in the N 1s spectra, however, BE predictions show that their presence or lack thereof can be easily determined from analyzing the Ti 2p peak. Point defects inducing positive BE shifts of the N 1s core electrons, like N vacancies and N split $(10\bar{1})$ -aligned interstitials, are predicted to be difficult to detect due to overlap with the satellite peak located at higher BE with respect to the main TiN N 1s component.

Table 2: Calculated directionally-averaged lattice parameter a , corresponding to the specific defect concentration of 1 per 64 atoms (in a reference perfect lattice) and its difference from the value for stoichiometric defect-free TiN (labeled as “none”).

defect type	a (Å)	Δa (Å)
none	4.239	0
V_N	4.239	< -0.001
V_{Ti}	4.230	-0.009
$I_N^{(10\bar{1})}$	4.267	0.028
$I_N^{(111)}$	4.268	0.029
I_N^t	4.267	0.028
$FP_N^{(10\bar{1})}$	4.267	0.028
$I_{Ti}^{(10\bar{1})}$	4.296	0.057
$I_{Ti}^{(111)}$	4.294	0.055
I_{Ti}^t	4.296	0.057

3.4.2. *Ab initio* lattice parameters

It was already shown that the lattice parameter can be one of the factors signaling the presence of point defects [16]. Table 2 shows the predicted impact of the studied point defects on the lattice parameter, which corresponds to the concentration of one defect per 64 atoms (in the reference perfect lattice). In general, at the studied defect concentration, N vacancies have no significant effect on the lattice parameter, while Ti vacancies reduce the lattice parameter by ~ 0.01 Å at the simulated vacancy concentration. N interstitial increases the lattice parameter by around 0.03 Å independent of the interstitial type, while an increase in lattice parameter of 0.06 Å is predicted for Ti interstitial and again does not depend on its type. N Frenkel pairs influence the lattice parameter in a similar way as N interstitials alone.

3.5. *Ti vacancy quantification*

Based on DFT calculations, the observed changes in the N 1s spectra with increasing off-stoichiometry can be explained by Ti vacancies, N tetrahedral interstitials or Ti interstitials. The formation of Ti interstitials can be ruled out, since they are predicted to exhibit a distinct fingerprints also in the Ti 2p spectra, with a well separated peak at lower binding energies, shifted by 1.5 – 2.3 eV with respect to the main TiN peak, and no such peak is observed in the here studied films as shown in Figure 3b). This is expected as the Ti interstitials have a high formation energies and are furthermore not favored by the N-rich film stoichiometry. On the contrary, the presence of both Ti vacancies and N tetrahedral interstitials is consistent with the film composition mea-

sured by the ion beam analysis (Table 1) and XRD (Figure 1) results. Only the tetrahedral N interstitials are predicted to be detectable in the XPS spectra. The split N interstitials are more stable than the tetrahedral ones [55], however, as HPPMS deposition is a highly energetic process, creating N tetrahedral interstitials cannot be ruled out. Because the N tetrahedral interstitials have a fingerprint that is indistinguishable from the fingerprint of the Ti vacancies, while the split N interstitials do not have a signal overlapping with the signal of Ti vacancies, it is important to estimate the respective N interstitial populations.

Results from our NEB calculations show, that the energy barrier E_a for the transition of N interstitial from the tetrahedral position to the geometrically closest (111) aligned split interstitial is only ~ 0.35 eV. The transition frequency can be calculated as

$$k = Ae^{-\frac{E_a}{k_B T}}. \quad (1)$$

where A is the attempt frequency, k_B is the Boltzmann constant and T is the temperature. Using the before-calculated activation energy together with a very crude estimate of the attempt frequency at 5 THz, based on the position of the first maximum in TiN phonon density of states [70], leads to transition frequency of 6.6 MHz at room temperature and 94 MHz at 100 °C. Hence, it is predicted that a large population of tetrahedral N interstitials is unlikely, even at room temperature and, therefore, the vast majority of the N interstitials are predicted to be the split ones, which have no distinct signal in the XPS N 1s spectra and are predicted to only lead to peak broadening of the main N 1s component (or would overlap with the satellite). Therefore, for the following analyses, it is reasonable to assume that all the N 1s XPS signal at the lower BE peaks originates from the presence of Ti vacancies.

For the Ti vacancy quantification in TiN_x , we adapt a method published previously by us for the analysis of Ti vacancies in TiON thin films [29]. A similar fitting procedure was used to fit the N 1s peak components, with the most notable difference is that there was no sign of the N_2 peak, so it was not included during the fitting. Four peaks were used for the fits, corresponding to the main TiN component (Ti atoms with 6 N neighbors and 0 vacancies, denoted 0V), two components at lower BEs corresponding to Ti atoms with 1 and 2 vacancies (denoted 1V and 2V) in the first coordination shell and a satellite peak. Approximate Voigt (Gaussian/Lorentzian) peakshapes in a product form [71]

$$GL(p_i) = \exp\left(-4 \ln 2(1 - p_i) \frac{(E - E_i)^2}{B_i^2}\right) / \left(1 + 4p_i \frac{(x - E)^2}{B^2}\right), \quad (2)$$

where E is energy, E_i is peak position, B_i is peak broadening parameter (its value is close to full width at half the maximum intensity), and p_i stands for fraction of the Lorentzian part in % of a peak i were employed. The GL(70) lineshape was used for the main TiN-like (0V) peak, while GL(30) line shapes were utilized for the 1V and 2V peaks and GL(0) for the satellite peak. Peak intensities, positions, and broadening were free-fitting parameters, however, only a single shared broadening parameter was fitted for the 1V and 2V peaks to reduce fit ambiguity. A Tougaard-like background shape was utilized during the fitting. The fits of the N 1s regions of all samples are shown in Figure 5, while the fit parameters are summarized in Table 3. Using this four-peak model, it was possible to achieve near-perfect fits for all the studied samples. Additionally, the fit parameters are very stable between the fits and the fitted peak positions are in good agreement with the predicted shifts. Specifically, the positions of the three main peaks are in the range of 397.12–397.19 eV, 396.49–396.52 eV, and 396.91–396.07 eV for the 0V, 1V, and 2V components, respectively. This is in excellent agreement with the here calculated value of -0.54 eV for the shift between 0V and 1V peak as well as the predicted and experimentally observed shifts between corresponding components in TiON [29].

The fitting was followed by a simplified version of the analysis of the relative peak ratios from [29], enabled by the fact that there is no oxidation of the TiN layer due to the Al capping, and, therefore, no need for corrections compensating the TiN oxidation. Vacancy concentration can be directly quantified from the three N 1s main components (0V, 1V, 2V) ratios. Assuming a cubic TiN monocrystal, i.e., neglecting the grain boundaries, with random vacancy distribution, the probability of finding an N atom with $6-n$ Ti first neighbors, or equivalently with n neighboring Ti vacancies, is [29]

$$P^{N^{nV_{\text{Ti}}}}(\delta) = \binom{6}{n} \delta^n (1 - \delta)^{6-n}, \quad (3)$$

where δ is the vacancy concentration on the metal sublattice.

During the vacancy quantification, we search for a δ which minimizes the squared differences between the experimental (fitted) $N^{nV_{\text{Ti}}}$ components and the theoretical ones, where both the experimental and theoretical functions were previously renormalized to sum to 1. Only the first three components are considered, i.e., corresponding to the N atoms with 0, 1, and 2 Ti vacancies in the first coordination shell. The normalization is needed for the experimental components, as opposed to using directly the fractions from Table 3, since the fit also includes the satellite peak. For the theoretical $P^{N^{nV_{\text{Ti}}}}(\delta)$ probabilities, the normalization is equivalent to neglecting the

Table 3: Fitted parameters for the fits shown in Figure 5. f_i , E_i and B_i correspond to peak fraction (of the total fitted area), peak position and peak broadening parameter for the i component.

sample	f_{TiN}	E_{TiN} (eV)	B_{TiN} (eV)
TiN _{1.37}	0.485(4)	397.123(2)	0.785(4)
TiN _{1.35}	0.577(3)	397.159(1)	0.714(2)
TiN _{1.23}	0.645(3)	397.1754(8)	0.686(2)
TiN _{1.18}	0.672(3)	397.1867(7)	0.665(2)
sample	f_{1v}	E_{1v} (eV)	B_{1v} (eV)
TiN _{1.37}	0.147(3)	396.495(4)	0.65(1)
TiN _{1.35}	0.106(2)	396.513(4)	0.6(1)
TiN _{1.23}	0.064(2)	396.51(5)	0.54(1)
TiN _{1.18}	0.044(2)	396.504(7)	0.48(2)
sample	f_{2v}	E_{2v} (eV)	B_{2v} (eV)
TiN _{1.37}	0.046(1)	395.916(8)	0.65(1)
TiN _{1.35}	0.0237(9)	395.95(1)	0.6(1)
TiN _{1.23}	0.016(1)	396.01(2)	0.54(1)
TiN _{1.18}	0.012(1)	396.07(2)	0.48(2)
sample	f_{satel}	E_{satel} (eV)	B_{satel} (eV)
TiN _{1.37}	0.322(3)	398.07(2)	3.42(3)
TiN _{1.35}	0.293(3)	398.22(2)	3.46(3)
TiN _{1.23}	0.274(3)	398.34(2)	3.48(4)
TiN _{1.18}	0.272(3)	398.38(2)	3.46(4)

components corresponding to the N atoms with more than two vacancies in the first coordination shell. There is no experimental evidence for a corresponding signal in our data and the probability of finding such configuration at small δ is very low; therefore, this is a reasonable simplification. This approach is consistent with that employed in Ref. [29], but it is significantly more robust due to the capping layer, eliminating the need for additional parameters to account for oxidation, which in turn reduces uncertainty.

The theoretical $P_{\text{norm}}^{\text{N}^m\text{V}^n\text{Ti}}(\delta)$ are shown in Figure 6 together with the fitted ratios for the four here studied samples. The x axis positions of the experimental points correspond to the fitted δ using the aforementioned procedure and is thus the determined Ti vacancy concentration on the metal sublattice.

We note that the N 1s fits and thus also the δ results are sensitive to the peak shapes used during the fitting. The specific combination of the used lineshapes described above was selected since it leads to fits with the lowest residual mean square errors. Furthermore, the notion of using

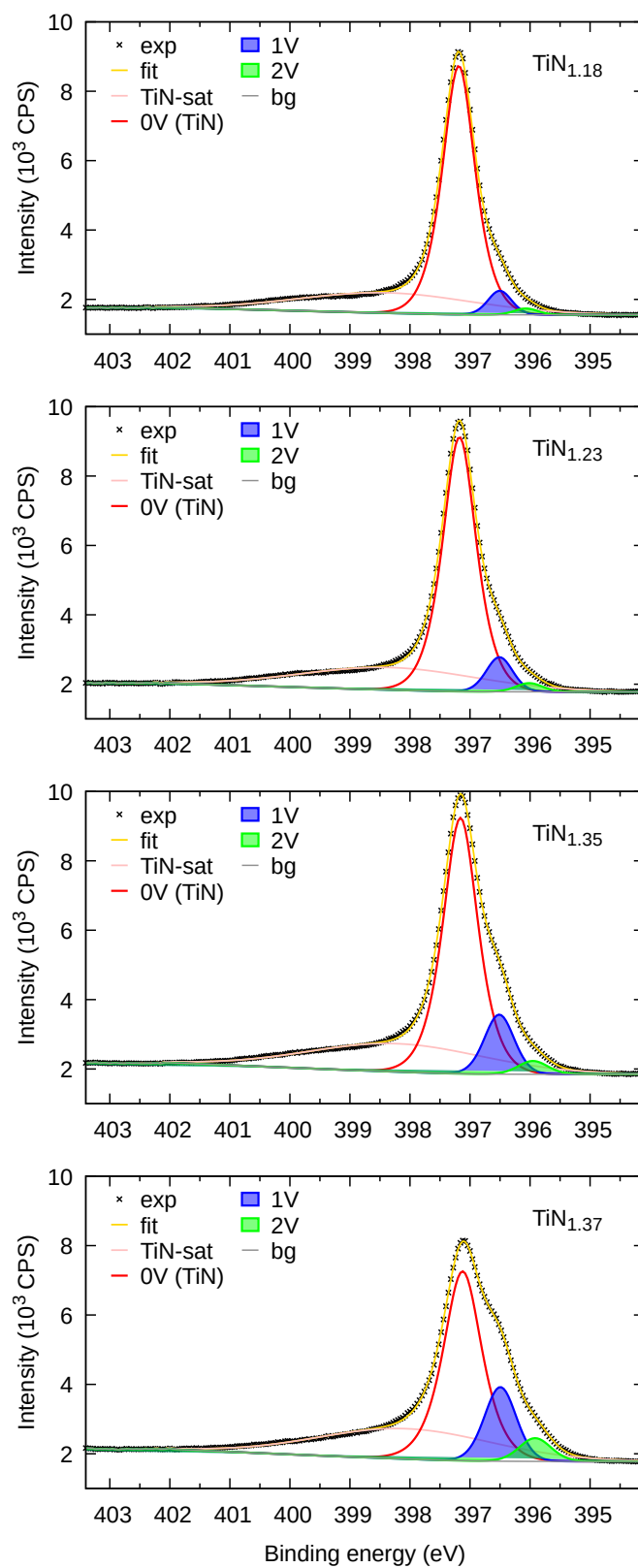


Figure 5: Fits of XPS N 1s spectra of all samples using the four-peak model discussed in the text.

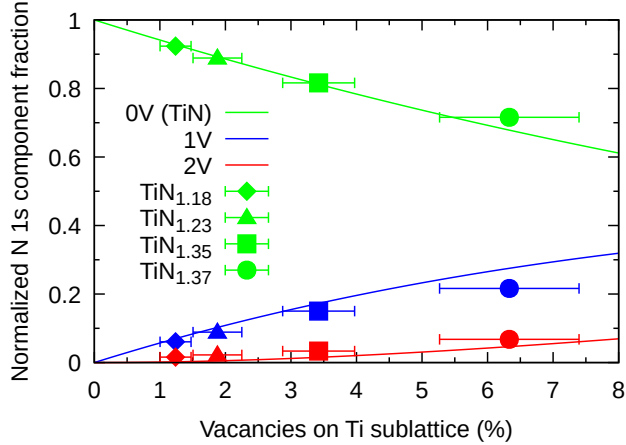


Figure 6: Continuous lines show theoretical $P_{\text{norm}}^{N^{0V\text{Ti}}}(\delta)$ (0 vacancies, 0V), $P_{\text{norm}}^{N^{1V\text{Ti}}}(\delta)$ (1 vacancy, 1V), and $P_{\text{norm}}^{N^{2V\text{Ti}}}(\delta)$ (2 vacancies, 2V) normalized functions corresponding to normalized probabilities to find N atom with 0, 1, and 2 Ti vacancies in the first coordination shell, assuming a random vacancy distribution. Points correspond to the fitted normalized peak ratios for the experimental TiN_x samples. Their x axis position is the determined vacancy concentration δ in the specific sample and x axis error bars visualize the δ uncertainty from the fit.

different peak shapes for the main TiN-like 0V peak is based already on previous work [42] where this peak was also fitted with a more Lorentzian peak shape. However, it is not immediately clear why a different lineshape should be needed for the main TiN-like component and 1V and 2V components. One possible explanation for the need for a different lineshape for the TiN component is the presence of interstitials. We have previously discussed that the presence of split N interstitials is likely and they would overlap with the main 0V peak and could contribute to a different broadening character. To estimate the uncertainty related to the used peak shapes we have also run several different fits, e.g., with GL(30) or GL(70) for all three main peaks and several other variants (GL(30) also for the satellite peak, GL(90) for the TiN-like peak, etc.). The average difference between the resulting δ values of different fits is 0.0025, with the maximum δ value difference between different fits was less than 0.01. Thus, this uncertainty due to peak shape selection is smaller than the δ uncertainty from the fit itself which is shown in Figure 6. Another possible source of uncertainty, the background shape choice (e.g., linear, Shirley, Tougaard) does not significantly influence the results due to a minimal increase of the background over the N 1s peak and thus its influence on the δ results is negligible.

4. Conclusions

Based on *ab initio* predictions, it is shown that several point defects in TiN, specifically Ti vacancies, N tetrahedral interstitials and Ti interstitials, induce N 1s and/or Ti 2p core electron

binding energy shifts in the first N and/or Ti neighbors, with a magnitude large enough to be detectable with standard laboratory X-ray photoelectron spectroscopy. The here presented calculations predict that significant N 1s BE shifts are associated with N tetrahedral interstitials and Ti vacancies, with N 1s shifts of -0.54 eV for first N neighbors of the Ti vacancy and N 1s shifts of -0.54 eV for first N neighbors of the tetrahedral N interstitial. However, while it is not possible to distinguish the Ti vacancies from N tetrahedral interstitials by the evaluation of N 1s binding energy shifts, we have also shown that the N tetrahedral interstitial is not stable at the room temperature. It quickly transform to the lower energy split interstitials and the population of tetrahedral N interstitials in TiN is negligible as a result. Therefore, we have shown that the N 1s signal at lower binding energies can be unambiguously attributed to Ti vacancies, Ti vacancies can be unambiguously detected in the XPS measurements of Al-capped TiN and the recently published XPS Ti vacancy quantification method for $\text{Ti}_{1-\delta}\text{O}_x\text{N}_{1-x}$ thin films can be adapted also for TiN films. This was successfully experimentally verified by XPS measurements of Al-capped TiN_x thin films with $1.18(5) \leq x \leq 1.37(5)$, where the Ti vacancy concentration on the metal sublattice ranged from 1.2(2) % to 6(1) %, respectively. The largest predicted Ti 2p BE shifts are associated with Ti interstitials, however no evidence for the formation of Ti interstitials was detected in the as deposited thin films. Hence, N rich TiN accommodates off-stoichiometry by both, formation of Ti vacancies as well as N split interstitials. Our results highlight that the *ab initio*-guided XPS-based point defect characterization method is suitable for the detection and quantification of several point defects in Al-capped TiN_x .

CRedit authorship contribution statement

Pavel Ondračka: Conceptualization, Formal analysis, Investigation, Methodology, Writing - original draft, review & editing, Visualization. Pauline Kümmerl: Investigation, Writing - original draft, review & editing, Marcus Hans: Investigation, Formal analysis, Writing - review & editing. Stanislav Mráz: Investigation, Writing - review & editing. Daniel Primetzhofer: Investigation, Formal analysis, Writing - review & editing. David Holec: Conceptualization, Investigation, Supervision, Writing - review & editing. Petr Vašina: Supervision, Writing - review & editing, Funding acquisition. Jochen M. Schneider: Conceptualization, Supervision, Project administration, Writing - review & editing, Funding acquisition.

Acknowledgments

This research was funded by German Research Foundation (DFG, SFB-TR 87/3) "Pulsed high power plasmas for the synthesis of nanostructured functional layer". This work was supported by the Ministry of Education, Youth and Sports of the Czech Republic through the e-INFRA CZ (ID:90254) and project LM2023039. The authors also gratefully acknowledge the computing time granted by the JARA Vergabegremium and provided on the JARA Partition part of the super-computer CLAIIX at RWTH Aachen University (project JARA0151) and computational resources provided by the e-INFRA CZ project (ID:90254), supported by the Ministry of Education, Youth and Sports of the Czech Republic. The NEB calculations have been achieved using the Vienna Scientific Cluster (VSC). Accelerator operation at Uppsala University has been supported by the Swedish research council VR-RFI (#2019_00191).

References

- [1] R. P. van Hove, I. N. Siervelt, B. J. van Royen, P. A. Nolte, Titanium-nitride coating of orthopaedic implants: A review of the literature, *BioMed Research International* 2015 (2015) 1–9. doi:10.1155/2015/485975.
- [2] P. Hedenqvist, M. Olsson, P. Wallén, A. Kassman, S. Hogmark, S. Jacobson, How TiN coatings improve the performance of high speed steel cutting tools, *Surface and Coatings Technology* 41 (2) (1990) 243–256. doi:10.1016/0257-8972(90)90172-9.
- [3] M. Nose, M. Zhou, E. Honbo, M. Yokota, S. Saji, Colorimetric properties of ZrN and TiN coatings prepared by DC reactive sputtering, *Surface and Coatings Technology* 142–144 (2001) 211–217. doi:10.1016/s0257-8972(01)01196-3.
- [4] E. Santecchia, A. Hamouda, F. Musharavati, E. Zalnezhad, M. Cabibbo, S. Spigarelli, Wear resistance investigation of titanium nitride-based coatings, *Ceramics International* 41 (9) (2015) 10349–10379. doi:10.1016/j.ceramint.2015.04.152.
- [5] L. Hultman, Thermal stability of nitride thin films, *Vacuum* 57 (1) (2000) 1–30. doi:10.1016/s0042-207x(00)00143-3.
- [6] Z. Lu, X. Liu, G. Hou, J. Chen, T. Zhu, J. Xu, K. Chen, Doping-free titanium nitride carrier selective contacts for efficient organic–inorganic hybrid solar cells, *ACS Applied Energy Materials* 3 (9) (2020) 9208–9215. doi:10.1021/acsaem.0c01517.

- [7] X. Yang, W. Liu, M. De Bastiani, T. Allen, J. Kang, H. Xu, E. Aydin, L. Xu, Q. Bi, H. Dang, E. AlHabshi, K. Kotsovos, A. AlSaggaf, I. Gereige, Y. Wan, J. Peng, C. Samundsett, A. Cuevas, S. De Wolf, Dual-function electron-conductive, hole-blocking titanium nitride contacts for efficient silicon solar cells, *Joule* 3 (5) (2019) 1314–1327. doi:10.1016/j.joule.2019.03.008.
- [8] Z. Li, H. Dai, X. Zhang, L. Ruan, J. Shi, T. Li, Y. Zhou, Porous titanium nitride nanowire array on carbon fiber for the applications in fiber-shaped solar cell and lithium-ion battery, *Journal of Energy Storage* 99 (2024) 113444. doi:10.1016/j.est.2024.113444.
- [9] C.-C. Chang, J. Nogan, Z.-P. Yang, W. J. M. Kort-Kamp, W. Ross, T. S. Luk, D. A. R. Dalvit, A. K. Azad, H.-T. Chen, Highly plasmonic titanium nitride by room-temperature sputtering, *Scientific Reports* 9 (1) (2019). doi:10.1038/s41598-019-51236-3.
- [10] A. Catellani, P. D’Amico, A. Calzolari, Tailoring the plasmonic properties of metals: The case of substoichiometric titanium nitride, *Physical Review Materials* 4 (1) (2020). doi:10.1103/physrevmaterials.4.015201.
- [11] U. Mahajan, M. Dhonde, K. Sahu, P. Ghosh, P. M. Shirage, Titanium nitride (TiN) as a promising alternative to plasmonic metals: a comprehensive review of synthesis and applications, *Materials Advances* 5 (3) (2024) 846–895. doi:10.1039/d3ma00965c.
- [12] G. V. Naik, V. M. Shalaev, A. Boltasseva, Alternative plasmonic materials: beyond gold and silver, *Advanced materials* 25 (24) (2013) 3264–3294. doi:10.1002/adma.201205076.
- [13] C. Mirguet, L. Calmels, Y. Kihn, Electron energy loss spectra near structural defects in TiN and TiC, *Micron* 37 (5) (2006) 442–448. doi:10.1016/j.micron.2005.11.012.
- [14] P. E. Schmid, M. Sato Sunaga, F. Lévy, Optical and electronic properties of sputtered TiN_x thin films, *Journal of Vacuum Science & Technology A: Vacuum, Surfaces, and Films* 16 (5) (1998) 2870–2875. doi:10.1116/1.581433.
- [15] G. B. Smith, P. D. Swift, A. Bendavid, TiN_x films with metallic behavior at high N/Ti ratios for better solar control windows, *Applied Physics Letters* 75 (5) (1999) 630–632. doi:10.1063/1.124463.

- [16] Z. Zhang, A. Ghasemi, N. Koutná, Z. Xu, T. Grünstäudl, K. Song, D. Holec, Y. He, P. H. Mayrhofer, M. Bartosik, Correlating point defects with mechanical properties in nanocrystalline TiN thin films, *Materials and Design* 207 (2021) 109844. doi:10.1016/j.matdes.2021.109844.
- [17] M. Guemmaz, A. Mosser, R. Ahuja, J. Parlebas, Theoretical and experimental investigations on elastic properties of substoichiometric titanium nitrides: influence of lattice vacancies, *International Journal of Inorganic Materials* 3 (8) (2001) 1319–1321. doi:10.1016/s1466-6049(01)00151-9.
- [18] T. Lee, K. Ohmori, C.-S. Shin, D. G. Cahill, I. Petrov, J. E. Greene, Elastic constants of single-crystal $\text{TiN}_x(001)$ ($0.67 \leq x \leq 1.0$) determined as a function of x by picosecond ultrasonic measurements, *Physical Review B* 71 (14) (2005). doi:10.1103/physrevb.71.144106.
- [19] C.-S. Shin, D. Gall, N. Hellgren, J. Patscheider, I. Petrov, J. E. Greene, Vacancy hardening in single-crystal $\text{TiN}_x(001)$ layers, *Journal of Applied Physics* 93 (10) (2003) 6025–6028. doi:10.1063/1.1568521.
- [20] J. Judek, P. Wróbel, P. P. Michałowski, M. Oźga, B. Witkowski, A. Seweryn, M. Struzik, C. Jastrzebski, K. Zberecki, Titanium nitride as a plasmonic material from near-ultraviolet to very-long-wavelength infrared range, *Materials* 14 (22) (2021) 7095. doi:10.3390/ma14227095.
- [21] D. Connétable, R. Besson, K. Gautier, E. Epifano, D. Monceau, First-principles study of point defects in ti–n compounds including oxygen insertion – consequences on oxidation of ti alloys, *The Journal of Physical Chemistry C* 128 (34) (2024) 14477–14499. doi:10.1021/acs.jpcc.4c03727.
- [22] J. Zimmermann, M. W. Finnis, L. C. Ciacchi, Vacancy segregation in the initial oxidation stages of the $\text{TiN}(100)$ surface, *The Journal of Chemical Physics* 130 (13) (2009). doi:10.1063/1.3105992.
- [23] N. K. Ponon, D. J. Appleby, E. Arac, P. King, S. Ganti, K. S. Kwa, A. O’Neill, Effect of deposition conditions and post deposition anneal on reactively sputtered titanium nitride thin films, *Thin Solid Films* 578 (2015) 31–37. doi:10.1016/j.tsf.2015.02.009.

- [24] A. S. Abiyev, E. M. Huseynov, M. N. Mirzayev, B. Mauvey, S. F. Samadov, Positron annihilation lifetime and doppler broadening spectroscopies studies of defects in nano tin crystal under gamma irradiation and high temperature, *Indian Journal of Physics* (May 2024). doi:10.1007/s12648-024-03229-w.
- [25] B. Qi, H. Gunnlaugsson, A. Mokhles Gerami, H. Gislason, S. Ólafsson, F. Magnus, T. Møllholt, H. Masenda, A. Tarazaga Martín-Lueugo, A. Bonanni, P. Krastev, V. Masondo, I. Unzueta, K. Bharuth-Ram, K. Johnston, D. Naidoo, J. Schell, P. Schaaf, ^{57}Fe Mössbauer study of epitaxial TiN thin film grown on MgO (100) by magnetron sputtering, *Applied Surface Science* 464 (2019) 682–691. doi:10.1016/j.apsusc.2018.09.107.
- [26] Z. Chen, Y. Huang, N. Koutná, Z. Gao, D. G. Sangiovanni, S. Fellner, G. Haberehner, S. Jin, P. H. Mayrhofer, G. Kothleitner, Z. Zhang, Large mechanical properties enhancement in ceramics through vacancy-mediated unit cell disturbance, *Nature Communications* 14 (1) (Dec. 2023). doi:10.1038/s41467-023-44060-x.
- [27] R. Qiu, H. Aboufadel, O. Bäcke, D. Stiens, H.-O. Andrés, M. Halvarsson, Atom probe tomography investigation of 3D nanoscale compositional variations in CVD TiAlN nanolamella coatings, *Surface and Coatings Technology* 426 (2021) 127741. doi:10.1016/j.surfcoat.2021.127741.
- [28] M. Hans, M. Tkadletz, D. Primetzhofer, H. Waldl, M. Schiester, M. Bartosik, C. Czettel, N. Schalk, C. Mitterer, J. M. Schneider, Is it meaningful to quantify vacancy concentrations of nanolamellar (ti, al)n thin films based on laser-assisted atom probe data?, *Surface and Coatings Technology* 473 (2023) 130020. doi:10.1016/j.surfcoat.2023.130020.
- [29] P. Ondračka, M. Hans, D. M. Holzapfel, D. Primetzhofer, D. Holec, J. M. Schneider, Ab initio-guided X-ray photoelectron spectroscopy quantification of Ti vacancies in $\text{Ti}_{1-\delta}\text{N}_{1-x}\text{O}_x$, *Acta Materialia* 230 (7) (2022) 117778. doi:10.1016/j.actamat.2022.117778.
- [30] T. Ozaki, C.-C. Lee, Absolute Binding Energies of Core Levels in Solids from First Principles, *Physical Review Letters* 118 (2) (2017) 026401. doi:10.1103/PhysRevLett.118.026401.
- [31] A. Aarva, V. L. Deringer, S. Sainio, T. Laurila, M. A. Caro, Understanding X-ray Spectroscopy of Carbonaceous Materials by Combining Experiments, Density Functional Theory,

- and Machine Learning. Part I: Fingerprint Spectra, *Chemistry of Materials* 31 (22) (2019) 9243–9255. doi:10.1021/acs.chemmater.9b02049.
- [32] J. M. Kahk, J. Lischner, Predicting core electron binding energies in elements of the first transition series using the Δ -self-consistent-field method, *Faraday Discussions* 236 (2022) 364–373. doi:10.1039/d1fd00103e.
- [33] A. Panepinto, D. Cornil, P. Guttman, C. Bittencourt, J. Cornil, R. Snyders, Fine Control of the Chemistry of Nitrogen Doping in TiO_2 : A Joint Experimental and Theoretical Study, *The Journal of Physical Chemistry C* 124 (31) (2020) 17401–17412. doi:10.1021/acs.jpcc.0c05003.
- [34] P. Ondračka, D. Nečas, M. Carette, S. Elisabeth, D. Holec, A. Granier, A. Goulet, L. Zajíčková, M. Richard-Plouet, Unravelling local environments in mixed TiO_2 - SiO_2 thin films by XPS and *ab initio* calculations, *Applied Surface Science* 510 (2020) 145056. doi:10.1016/j.apsusc.2019.145056.
- [35] R. T. Haasch, T. Y. Lee, D. Gall, J. E. Greene, I. Petrov, Epitaxial $\text{TiN}(001)$ Grown and Analyzed In situ by XPS and UPS. I. Analysis of As-deposited Layers, *Surface Science Spectra* 7 (3) (2000) 193–203. doi:10.1116/1.1365617.
- [36] C. Walker, S. Morton, N. Brown, J. Matthew, High-resolution $\text{AlK}\alpha$ and high-photon energy $\text{CrK}\beta$ -excited X-ray photoelectron spectroscopy of titanium nitride, *Journal of Electron Spectroscopy and Related Phenomena* 95 (2-3) (1998) 211–223. doi:10.1016/S0368-2048(98)00211-4.
- [37] R. T. Haasch, T. Y. Lee, D. Gall, J. E. Greene, I. Petrov, Epitaxial $\text{TiN}(001)$ Grown and Analyzed In situ by XPS and UPS. II. Analysis of Ar + Sputter Etched Layers, *Surface Science Spectra* 7 (3) (2000) 204–212. doi:10.1116/1.1367596.
- [38] D. Jaeger, J. Patscheider, Single Crystalline Oxygen-free Titanium Nitride by XPS, *Surface Science Spectra* 20 (1) (2013) 1–8. doi:10.1116/11.20121107.
- [39] I. Milošev, H. H. Strehblow, B. Navinšek, XPS in the study of high-temperature oxidation of CrN and TiN hard coatings, *Surface and Coatings Technology* 74-75 (PART 2) (1995) 897–902. doi:10.1016/0257-8972(95)08360-X.

- [40] M. Kuznetsov, J. Zhuravlev, V. Gubanov, XPS analysis of adsorption of oxygen molecules on the surface of Ti and TiN_x films in vacuum, *Journal of Electron Spectroscopy and Related Phenomena* 58 (3) (1992) 169–176. doi:10.1016/0368-2048(92)80016-2.
- [41] G. Greczynski, S. Mráz, L. Hultman, J. M. Schneider, Venting temperature determines surface chemistry of magnetron sputtered TiN films, *Applied Physics Letters* 108 (4) (2016). doi:10.1063/1.4940974.
- [42] G. Greczynski, L. Hultman, Self-consistent modelling of X-ray photoelectron spectra from air-exposed polycrystalline TiN thin films, *Applied Surface Science* 387 (2016) 294–300. doi:10.1016/j.apsusc.2016.06.012.
- [43] G. C. Smith, A. B. Hopwood, K. J. Titchener, Electron inelastic mean free path for Ti, TiC, TiN and TiO₂ as determined by quantitative reflection electron energy-loss spectroscopy, *Surface and Interface Analysis* 33 (3) (2002) 230–237. doi:10.1002/sia.1205.
- [44] M. Delfino, J. A. Fair, D. Hodul, X-ray photoemission spectra of reactively sputtered TiN, *Journal of Applied Physics* 71 (12) (1992) 6079–6085. doi:10.1063/1.350465.
- [45] D. Jaeger, J. Patscheider, A complete and self-consistent evaluation of XPS spectra of TiN, *Journal of Electron Spectroscopy and Related Phenomena* 185 (11) (2012) 523–534. doi:10.1016/j.elspec.2012.10.011.
- [46] G. Greczynski, I. Petrov, J. E. Greene, L. Hultman, Al capping layers for nondestructive x-ray photoelectron spectroscopy analyses of transition-metal nitride thin films, *Journal of Vacuum Science & Technology A: Vacuum, Surfaces, and Films* 33 (5) (2015) 05E101. doi:10.1116/1.4916239.
- [47] G. Greczynski, D. Primetzhofer, J. Lu, L. Hultman, Core-level spectra and binding energies of transition metal nitrides by non-destructive x-ray photoelectron spectroscopy through capping layers, *Applied Surface Science* 396 (2017) 347–358. doi:10.1016/j.apsusc.2016.10.152.
- [48] P. Ström, D. Primetzhofer, Ion beam tools for nondestructive in-situ and in-operando composition analysis and modification of materials at the Tandem Laboratory in Uppsala, *Journal of Instrumentation* 17 (04) (2022) P04011. doi:10.1088/1748-0221/17/04/p04011.

- [49] Y. Zhang, H. J. Whitlow, T. Winzell, I. F. Bubb, T. Sajavaara, K. Arstila, J. Keinonen, Detection efficiency of time-of-flight energy elastic recoil detection analysis systems, *Nuclear Instruments and Methods in Physics Research Section B: Beam Interactions with Materials and Atoms* 149 (4) (1999) 477–489. doi:10.1016/s0168-583x(98)00963-x.
- [50] P. Ström, P. Petersson, M. Rubel, G. Possnert, A combined segmented anode gas ionization chamber and time-of-flight detector for heavy ion elastic recoil detection analysis, *Review of Scientific Instruments* 87 (10) (2016). doi:10.1063/1.4963709.
- [51] M. S. Janson, CONTES instruction manual, Internal Report, Uppsala University (2004).
- [52] M. to Baben, M. Hans, D. Primetzhofer, S. Evertz, H. Ruess, J. M. Schneider, Unprecedented thermal stability of inherently metastable titanium aluminum nitride by point defect engineering, *Materials Research Letters* 5 (3) (2016) 158–169. doi:10.1080/21663831.2016.1233914.
- [53] M. Moro, B. Bruckner, P. Grande, M. Tabacniks, P. Bauer, D. Primetzhofer, Stopping cross section of vanadium for H^+ and He^+ ions in a large energy interval deduced from backscattering spectra, *Nuclear Instruments and Methods in Physics Research Section B: Beam Interactions with Materials and Atoms* 424 (2018) 43–51. doi:10.1016/j.nimb.2018.03.032.
- [54] M. Mayer, SIMNRA, a simulation program for the analysis of NRA, RBS and ERDA, in: *AIP Conference Proceedings*, AIP, 1999, pp. 541–544. doi:10.1063/1.59188.
- [55] L. Tsetseris, N. Kalfagiannis, S. Logothetidis, S. T. Pantelides, Structure and interaction of point defects in transition-metal nitrides, *Physical Review B* 76 (22) (2007) 224107. doi:10.1103/PhysRevB.76.224107.
- [56] D. G. Sangiovanni, B. Alling, P. Steneteg, L. Hultman, I. A. Abrikosov, Nitrogen vacancy, self-interstitial diffusion, and Frenkel-pair formation/dissociation in *B1* TiN studied by *ab initio* and classical molecular dynamics with optimized potentials, *Physical Review B* 91 (5) (2015) 054301. doi:10.1103/PhysRevB.91.054301.
- [57] G. Kresse, J. Furthmüller, Efficiency of *ab-initio* total energy calculations for metals and semiconductors using a plane-wave basis set, *Computational Materials Science* 6 (1) (1996) 15–50. doi:10.1016/0927-0256(96)00008-0.

- [58] G. Kresse, J. Furthmüller, Efficient iterative schemes for *ab initio* total-energy calculations using a plane-wave basis set, *Physical Review B* 54 (16) (1996) 11169–11186. doi:10.1103/PhysRevB.54.11169.
- [59] P. Hohenberg, W. Kohn, Inhomogeneous Electron Gas, *Physical Review* 136 (3B) (1964) B864–B871. doi:10.1103/PhysRev.136.B864.
- [60] W. Kohn, L. J. Sham, Self-Consistent Equations Including Exchange and Correlation Effects, *Physical Review* 140 (4A) (1965) A1133–A1138. doi:10.1103/PhysRev.140.A1133.
- [61] G. Kresse, D. Joubert, From ultrasoft pseudopotentials to the projector augmented-wave method, *Physical Review B* 59 (3) (1999) 1758–1775. doi:10.1103/PhysRevB.59.1758.
- [62] H. Jónsson, G. Mills, K. W. Jacobsen, Nudged elastic band method for finding minimum energy paths of transitions, in: *Classical and Quantum Dynamics in Condensed Phase Simulations*, World Scientific Publishing, 1998, pp. 385–404. doi:10.1142/9789812839664_0016.
- [63] P. Blaha, K. Schwarz, F. Tran, R. Laskowski, G. K. H. Madsen, L. D. Marks, WIEN2k: An APW+lo program for calculating the properties of solids, *The Journal of Chemical Physics* 152 (7) (2020) 074101. doi:10.1063/1.5143061.
- [64] J. P. Perdew, K. Burke, M. Ernzerhof, Generalized Gradient Approximation Made Simple, *Physical Review Letters* 77 (18) (1996) 3865–3868. doi:10.1103/PhysRevLett.77.3865.
- [65] M. Scheidgen, L. Himanen, A. N. Ladines, D. Sikter, M. Nakhaee, A. Fekete, T. Chang, A. Golparvar, J. A. Márquez, S. Brockhauser, S. Brückner, L. M. Ghiringhelli, F. Dietrich, D. Lehmborg, T. Denell, A. Albino, H. Näsström, S. Shabih, F. Dobener, M. Kühbach, R. Mozumder, J. F. Rudzinski, N. Daelman, J. M. Pizarro, M. Kuban, C. Salazar, P. Ondračka, H.-J. Bungartz, C. Draxl, NOMAD: A distributed web-based platform for managing materials science research data, *Journal of Open Source Software* 8 (90) (2023) 5388. doi:10.21105/joss.05388.
- [66] Ondračka Pavel, NOMAD dataset: Prediction and identification of point defect fingerprints in the X-ray photoelectron spectra of TiN_x (2024). doi:10.17172/NOMAD/2024.03.28-1. URL <https://nomad-lab.eu/prod/v1/gui/dataset/doi/10.17172/NOMAD/2024.03.28-1>

- [67] K. Balasubramanian, S. V. Khare, D. Gall, Energetics of point defects in rocksalt structure transition metal nitrides: Thermodynamic reasons for deviations from stoichiometry, *Acta Materialia* 159 (2018) 77–88. doi:10.1016/j.actamat.2018.07.074.
- [68] K. Momma, F. Izumi, VESTA 3 for three-dimensional visualization of crystal, volumetric and morphology data, *Journal of Applied Crystallography* 44 (6) (2011) 1272–1276. doi:10.1107/S0021889811038970.
- [69] M. Tsujimoto, H. Kurata, T. Nemoto, S. Isoda, S. Terada, K. Kaji, Influence of nitrogen vacancies on the N K-ELNES spectrum of titanium nitride, *Journal of Electron Spectroscopy and Related Phenomena* 143 (2-3) (2005) 159–165. doi:10.1016/j.elspec.2004.04.006.
- [70] S. K. Gupta, S. D. Gupta, H. R. Soni, V. Mankad, P. K. Jha, First-principles studies of the superconductivity and vibrational properties of transition-metal nitrides TMN (TM = Ti, V, and Cr), *Materials Chemistry and Physics* 143 (2) (2014) 503–513. doi:10.1016/j.matchemphys.2013.08.046.
- [71] S. Evans, Curve synthesis and optimization procedures for x-ray photoelectron spectroscopy, *Surface and Interface Analysis* 17 (2) (1991) 85–93. doi:10.1002/sia.740170204.